Application of three-dimensional fault stress models for assessment of fault stability for CO2 storage sites

Gamboa, Davide; Williams, John D. O.; Bentham, Michelle; Schofield, David I.; Mitchell, Andy

Published in:
International Journal of Greenhouse Gas Control

DOI:
10.1016/j.ijggc.2019.102820

Publication date:
2019

Citation for published version (APA):
Gamboa, D., Williams, J. D. O., Bentham, M., Schofield, D. I., & Mitchell, A. (2019). Application of three-dimensional fault stress models for assessment of fault stability for CO2 storage sites. *International Journal of Greenhouse Gas Control*, *90*, [102820]. https://doi.org/10.1016/j.ijggc.2019.102820

Application of three-dimensional fault stress models for assessment of fault stability for CO_2 storage sites

Davide Gamboa[12*], John Williams[3], Michelle Bentham[3], David Schofield[4], Andrew C. Mitchell[5]

[1]Current address: Instituto Português do Mar e da Atmosfera (IPMA), Rua C ao Aeroporto Humberto Delgado, 1749-077 Lisboa, Portugal

[2]British Geological Survey, Cardiff University Main Building, Cardiff, CF10 3AT, United Kingdom.

[3]British Geological Survey, Keyworth, Nottinghamshire, NG12 5GU, United Kingdom.

[4]British Geological Survey, The Lyell Centre, Research Avenue South, Edinburgh, EH14 4AP, United Kingdom

[5]Department of Geography and Earth Sciences, Aberystwyth University, Llandinam Building, Penglais Campus, Aberystwyth, SY23 3DB, United Kingdom

*Corresponding author: davide.gamboa@ipma.pt

Abstract

Carbon Capture and Storage (CCS) is a key technology for a low-carbon energy future and will have an important role on the economic future of the UK Continental Shelf (UKCS). The East Irish Sea Basin (EISB) is a prospective area for CCS in the western UKCS. 3D seismic from the EISB were used in this study to characterise the fault network and potential fault reactivation risks associated with CO_2 injection. Two main structural domains are present: a Northern domain with NW-SE faults, and a Southern domain with faults following a N-S orientation. The main storage sites consist of structural closures in Triassic strata of the Sherwood Sandstone Formation (SSF), overlain by alternations of mudstones and evaporites of the Triassic Mercia Mudstone Group (MMG). The closures occur predominantly at fault-bounded horsts, with adjacent grabens filled by thick sequences of the Triassic Mercia Mudstone Group (MMG). The fault framework was used to test, in 3D, the stress model published for the EISB and assess the fault reactivation risk associated to CO_2 storage. Slip tendency values were predominantly below 0.6, suggesting the presence of stable structures in the EISB. Under the tested conditions, faults are capable of withstanding pressure increases between 3 MPa and 10 MPa before the onset of slip. The limited fault reactivation risk suggests CCS operations are suitable prospects for the EISB. This work demonstrates the additional value gained from integration of accurately constrained fault geometries in 3D stress models.

Keywords: Carbon Capture and Sequestration, CCS, fault stress, stress model, East Irish Sea, UKCS

1. Introduction

Carbon capture and storage (CCS) is a key technology with potential to mitigate against the effects of global warming by reducing greenhouse gas emissions, and is required to meet targeted CO_2 reductions at least cost (Bradshaw and Cook, 2001; Gibbins and Chalmers, 2008; Haszeldine, 2009;

IEAGHG, 2017a; IPCC, 2011). The short-term targets for CCS are thermal power plants and carbon intensive industries, but carbon sequestration also plays a role in biomass and hydrogen systems that aspire toward neutral emissions scenarios (Azar et al., 2010; Damen et al., 2007; Gough and Upham, 2011; Marbán and Valdés-Solís, 2007). CCS operations aim to achieve the reduction of CO_2 released to the atmosphere by capturing it at major sources and safely injecting it in deep subsurface geological formations. These consist of rocks suitable to retain fluids, such as depleted hydrocarbon reservoirs or deep saline aquifers which are overlain by impermeable cap rocks able to retain the fluids in the reservoir (Benson and Cole, 2008; Bentham and Kirby, 2005; Chadwick et al., 2006; IEAGHG, 2011; IPCC, 2011; RISCS, 2014). Large offshore sedimentary basins currently constitute a main target for CCS, as these comprise wide areas containing suitable lithologies with adequate porosity and permeability (Bachu, 2015; Bachu et al., 2007; Baines and Worden, 2004; Benson and Cole, 2008; Halland et al., 2013; Schrag, 2009). As these basins have been widely targeted for hydrocarbon exploration, there is often a much wider coverage of high-quality data, including 3D seismic, when compared to onshore areas.

The offshore domain of the East Irish Sea Basin (EISB) (Figure 1a) has been the target for hydrocarbon exploration since the late 1960s, having met significant exploration success during the 1970's with the discovery of hydrocarbon fields hosted in lithologies from the Sherwood Sandstone Group (Bunce, 2018; Colter, 1997; Haig et al., 1997; Ward and Baker, 2018; Yaliz and Taylor, 2003). With the oil and gas fields entering their mature phase and with a predicted end of production in the coming decade there is the opportunity to reform them as storage sites for CCS (Kirk, 2006; Li et al., 2006; Reynolds et al., 2018). Furthermore, the storage capacity of the EISB is extended beyond that of the hydrocarbon fields through potential utilisation of saline aquifer structures in the Sherwood Sandstone Group (Kirk, 2006) and Permian sandstones units (Gamboa et al., 2016). Thus, the EISB is a key player for the large-scale CCS deployment in the western UK, able to store CO_2 emissions from nearby major power plants, from industrial emitters from North Wales and Northwest England, and possibly from source points from South Wales. In addition to this, CCS on the EISB has gained a great momentum with the expected implementation of hydrogen energy networks in the northwestern United Kingdom, where natural gas is de-carbonated to hydrogen before distribution in gas networks that propose to use the offshore fields for CO_2 storage (Dodds and Demoullin, 2013).

A key safety criterion for storage sites is constraining the risk of CO_2 leakage based on the characterisation of faults bounding the known reservoirs and closures. The presence of fault networks is one of the main risks that can affect sub-surface storage operations as these can either behave as barriers or conduits for fluid flow (Aydin, 2000; Bachu and Grobe, 2006; IEAGHG, 2016; Nicol et al., 2017). The latter is crucial for CCS safety if the faults constitute permeable pathways for CO_2 to escape from the storage site. Fault permeability can be linked to their stress state, rock properties and geometry (Aydin, 2000; Ferrill and Morris, 2002; Morris et al., 1996; Nelson et al., 2005; Nicol et al., 2017; Sibson, 1996). Hence, it is crucial to assess the pressure conditions that lead to fault reactivation due to elevated pore pressure during fluid injection. This is a major consideration for CCS appraisal studies (Bretan et al., 2011; Roberts et al., 2017; Williams et al., 2016), as fault reactivation may induce the unwanted escape of fluids or induce seismicity through fault slip (IEAGHG, 2016; Mazzoldi et al., 2012; Nicol et al., 2017). These often occur in association, with fluids escaping partially through open pathways synchronous with the slip event (Sibson, 1995). The newly open flow paths can remain open, constituting active flow paths for variable time spans. The characterisation of fault properties in caprock strata is of particular relevance, as these

structures may have a strong impact on the likely integrity of fluid traps, potentially allowing the development of fluid flow bypass systems through the seal units (Cartwright et al., 2007; IEAGHG, 2017b; Maia et al., 2016; Petrie et al., 2014). At a regional scale, the location of faults can be interpreted on 3D seismic data, allowing broad scale mapping of networks and other fluid-flow features (Backe et al., 2015; Streit et al., 2005; Williams et al., 2018). Reliably constraining other properties such as *in situ* stress relies upon a high density of subsurface data obtained from boreholes (Sibson, 1995; Williams et al., 2018). Because these data tend to be obtained in the vicinity of target structural closures where boreholes are drilled to evaluate hydrocarbon reservoirs, these storage sites are well characterised from geological and geomechanical perspectives (Bentham et al., 2014; Firoozabadi and Cheng, 2010; Li et al., 2006). Consequently, undrilled closures in saline aquifers that can constitute storage sites for CO_2 tend to be less well characterised (Bachu et al., 2007; Bentham and Kirby, 2005). However, the geomechanical conditions estimated from boreholes can be extrapolated to non-drilled areas. This allows regional evaluations for the storage potential of a basin, and provide early stage indicators of the overall leakage risk in the vicinities of storage sites.

Williams et al. (2018) presented an *in situ* stress model for the offshore domains of the East Irish Sea based on borehole data, thus complementing a wealth of onshore data from location bordering the basin (e.g. Kingdon et al., 2016). However, the stress model for the offshore areas presented a very conservative approach to fault reactivation by only assuming vertical faults, therefore many faults returned high slip tendency values. To address this limitation, we here applying the parameters defined by Williams et al. (2018) to a detailed 3D fault network mapped from seismic data from the EISB. We here show how fault reactivation parameters change as a function of the fault 3D geometry on non-vertical faults, and how they can be impacted by data uncertainty involved in stress models. The key aim is to understand how much overpressure faults can theoretically withstand, with relevant implications for development planning of CCS operation in the western United Kingdom.

2. Geological overview

The East Irish Sea Basin (EISB) is one of the largest and deepest post-Carboniferous basins of Western Britain (Fig. 1, Jackson et al., 1995). Its present form was generated by E–W to NW–SE extension associated with Permian–Triassic rifting events, which gave rise to a series of N–S striking grabens and structural highs (Chadwick et al., 1994; Jackson et al., 1995; Needham and Morgan, 1997). The oldest rocks in the EISB are thought to be of Carboniferous or Late Devonian age (Fig. 1b and 2) and were deposited in NNW–SSE extensional basins, later folded along E–W Caledonian structures during the Variscan Orogeny. The top of the Carboniferous is marked by a regional angular unconformity over which continental sandstones of the Early Permian Collyhurst Sandstone Formation were deposited in narrow half-grabens. Upper Permian marine incursions resulted in sedimentation styles characteristic of coastal sabkhas, while halites and anhydrites of the St Bees Evaporite Formation were deposited in the central parts of the EISB. Towards the south, the Upper Permian evaporitic rocks thin and abruptly transition to mudstones of the Manchester Marls Formation (Jackson et al., 1995; Jackson et al., 1997).

The principal hydrocarbon reservoir unit in the basin is the Early Triassic Sherwood Sandstone Group (SSG, Bunce, 2018; Knipe et al., 1993). This was deposited in a predominantly fluvial environment

with a transition to an aeolian setting towards the top (Jackson et al., 1997). The overlying Mercia Mudstone Group (MMG) forms the main caprock to the EISB reservoir rocks, comprising alternating mudstones, siltstones, dolomites and evaporites deposited during the Late Triassic (Figure 2). The preserved thickness of MMG is highly variable, and is locally significantly thinned or absent due to erosion. This can pose a risk to the fluid retention system in affected areas, however up to 3200 m of MMG are preserved in the Keys Basin. The distribution and thickness of halite members within the EISB was controlled in part by local faulting and areas of high subsidence and is also highly variable (Jackson et al., 1995; Jackson and Mulholland, 1993; Wilson, 1990). The majority of the post-Triassic succession is virtually absent in the EISB due to erosion following regional uplift and basin inversion (Chadwick et al., 1994; Hillis et al., 2008; Holford et al., 2009).

Jackson & Mulholland (1993) recognised two main structural domains in the EISB, strictly related to the presence or absence of the late Permian St. Bees Evaporite Formation (Figure 1b and 3). The Southern Domain is characterised by closely spaced, N–S striking steep faults where Permian evaporites are absent. The faults in this domain often propagate through Permian and Triassic strata, bounding parallel arrays of tilted faults blocks (Figure 3c). The majority of the faults on the Southern domain terminate within early Permian strata, although in some cases these propagate into, or link with, underlying Carboniferous strata and structures (Figure 3c). The Northern domain is characterised by NW-SE trending faults, with lower dips compared to faults in the southern domain (Figure 1b, 3a and 3b). The late Permian evaporites control the vertical propagation of faults in this domain, acting as detachment levels to listric faults bounding large half-grabens and limiting the downward propagation of other fault cutting the Triassic seal and reservoir successions (Figure 3b).

3. Methods

3.1 Seismic interpretation and depth conversion

This study is based on use of combined 3D seismic surveys that cover an area of 1850 Km^2 on the southern/central EISB (Figure 1a). The seismic interpretation process focused on the regional mapping of key reference reflectors, the Top SSG and Top Permian, and of 205 faults identified within the 3D survey limits (Figure 3). Geological faults are identified as sub-vertical, planar to arched discontinuities with variable dip angles visualised on the seismic profiles (Figure 3), and mapping this structures in 3D reveals detailed changes along the fault plane geometry. Sufficient well-log data were available to allow correlation of the 3D seismic data with stratigraphic markers of interest at depth. Thus, the faults mapped on seismic data volumes in the time domain where were converted to depth domain to provide higher accuracies in fault dip angles. A constant velocity of 1500 m/s was used for the water column, while available sonic logs were used to estimate the average velocity of intervals within the subsurface. Two main stratigraphic intervals were defined (Figure 3). Interval 1 comprises the shallow subsurface levels and Mercia Mudstone Formation (between the seafloor and Top SSG horizon). Interval 2 comprises the lower Triassic strata (between the Top SSG and Top Permian horizons). The average velocities obtained at each borehole were gridded to obtain lateral velocity variation for each defined interval and to produce a simplified depth model.

3.2. Stress vector characterisation

The *in situ* stress state in the subsurface is described as three main orthogonal principal components: the maximum (S_1), the intermediate (S_2) and minimum (S_3) principal stresses. If one of the main stress components is (sub) vertical, it can be expressed as vertical stress (S_v) approximating to the weight of the overburden. Consequently, the horizontal stress components are referred to as S_{Hmax}, the maximum principal horizontal stress; and S_{hmin}, the minimum principal horizontal stress (Zoback, 2010). The relative magnitude between stress components depends on the geological setting and prevalent stress regimes, which can be extensional faulting ($S_v >= S_{Hmax} >= S_{hmin}$), compressional faulting ($S_{Hmax} >= S_{hmin} >= S_v$) or strike-slip ($S_{Hmax} >= S_v >= S_{hmin}$) (Zoback, 2010).

Characterising the main stress components is crucial to producing accurate subsurface stress models. This procedure requires estimation of both subsurface pore-pressure gradients and the orientation and magnitude of the three principal stress components. The magnitude of the vertical stress S_v is constrained by the weight of the subsurface rocks and fluids and is estimated in offshore settings

by integrating data from bulk density logs through Equation 1 (Chiaramonte et al., 2008; Engelder, 1993; Zoback, 2010). This accounts for a water column component and a subsurface rock density component. Here ρ_w and Z_w are respectively water density (considered as 1 g/cm^3) and depth, $\rho(Z)$ is rock density as a function of depth, $\bar{\rho}$ is the overburden mean density and g is the acceleration due to gravity.

$$S_v = \rho_w g Z_w + \int_{Z_w}^{Z} \rho(Z) g \, dz = \rho_w g Z_w + \bar{\rho} g (Z - Z_w) \quad \text{Equation 1}$$

The orientation of the minimum horizontal stress, $S_{hmin,}$ is determined through the identification of borehole breakouts and drilling-induced tensile fractures visualised on image logs. Breakouts occur when the maximum stress around the hole is large enough to exceed the strength of the rock, causing the borehole to fail in compression along the orientation of S_{hmin} (Tiab and Donaldson, 2015; Zoback, 2010). The orientation of S_{HMax} is thus perpendicular to the minimum horizontal stress orientation, often represented on image logs by drilling-induced tensile fractures of limited vertical extent. These form on opposite sides of the borehole wall at 90 degrees to the borehole breakouts (Zoback, 2010). The magnitude of the minimum horizontal stress can be estimated through leak-off tests (LOT), which induce small-scale hydraulic fractures during pumping tests on open sections of the well and can be used to estimate the magnitude of the least principal stress at particular depths (Zoback, 2010).

The magnitude of the maximum horizontal stress cannot be directly measured. Methods have been developed to estimate it by calculating the general frictional limits of stress needed to initiate fault reactivation by assuming a ratio between the maximum and minimum horizontal stress magnitudes. Knowing S_{hmin}, pore pressure gradients *Pp* and the coefficient of friction μ (often referred as the fault "strength"), an upper bound for S_{Hmax} magnitude can be obtained using coefficient of friction values under which slip occurs on a cohesionless fault. These coefficients typically fall within values between 0.6 and 0.85 for critically stressed faults (Barton et al., 1995; Ferrill et al., 2017; Streit et al., 2005; Zoback, 2010). Given the strike-slip dominant state of stress determined for the western UK (Baptie, 2010; Fellgett et al., 2018; Williams et al., 2018), S_{Hmax} (S1) is

the maximum principal stress, the S_v the intermediate and S_{hmin} (S3) the least stress component. The maximum bound for S_{Hmax} is estimated using equation 2, where σ_1 and σ_3 account for the maximum and minimum horizontal stresses and Pp for the pore pressure:

$$\frac{\sigma_1}{\sigma_3} = \frac{S1-Pp}{S3-Pp} \leq [(\mu^2+1)^{\frac{1}{2}} + \mu]^2 \qquad \text{Equation 2}$$

3.3. Fault stress modelling

With knowledge of the the orientation and magnitude of the three principal stress components and pore pressure gradients, it is possible to model the reactivation conditions of pre-existing faults. The first step is to define in detail the fault geometry. These complex surfaces cannot be simplified as single planes with uniform orientation and dip. Thus, the fault surfaces mapped on the seismic data are converted into a mesh surface composed of numerous smaller polygons that closely represents the real morphology (Fig. 4). Meshed surfaces from 3D fault planes represented in stereographic projections will therefore produce a range of dip and azimuth values derived from the fault's rugosity. These data are represented on stereographic diagrams as poles perpendicular to the main planes for a clearer trend visualisation of trends when very high numbers are represented (Figure 4). One key aspect to consider is that, due to the perpendicular relationship between planes and their poles, points represented on the western quadrant represent east-dipping planes, and vice-versa.

The stress tensor acting on a plane can be divided into normal stress and shear stress components (Figure 4). Fault slip occurs when the shear stress exceeds the normal stress acting on a fault surface (Lisle and Srivastava, 2004; Morris et al., 1996). Faults oriented 30 degrees to the maximum principal stress are generally the most prone to reactivate as they possess the highest shear to normal stress ratios (Sibson, 1985). Rock failure limit conditions can be represented as a function of the confining stress using a Mohr-Coulomb failure envelope and Mohr circles (Barton et al., 1995; Morris et al., 1996; Zoback, 2010) (Figure 4). The Mohr circle illustrates the difference between the effective maximum and minimum principal stresses. Increasing pore pressure during fluid injection will therefore reduce the effective stresses, moving the Mohr circle towards the failure envelope. Failure occurs once the circle intersects the failure envelope (Figure 4).

A series of parameters can be determined to estimate fault reactivation behaviour as a function of their orientation, the shear to normal stress ratios and pore pressure. Here we use fault Slip Tendency and Fracture stability to assess reactivation associated with the regional fault network mapped in the East Irish Sea Basin (Figure 5). Faults are likely to slip when the ratio between the stress components exceeds the frictional resistance of sliding. The Slip Tendency (T_s) of a fault provides a proxy to assess fault slip, being defined as the ratio of shear (τ) to normal stress (σ_n) acting on an oriented surface subjected to a stress field (Equation 3), independently of friction or cohesion information (Ferrill et al., 2017; Morris et al., 1996). Slip tendency values allow the assessment of the likelihood and direction of slip on the fault surface analysed, and can be used as proxies for fault displacement (Mcfarland et al., 2012). When applied to a 3D mesh surface, each individual polygon will have a slip tendency value but as a whole these illustrate the spatial changes of attributes along the fault planes.

$T_s = \tau/\sigma_n$ Equation 3

The *Fracture Stability* estimates the increase in pore pressure (ΔP) that is required for a fault plane to slip, i.e. to reach the failure envelope (Figure 4c), due to decreasing effective stresses while taking into account cohesion and tensile strenght (Sibson, 2003). The Fracture Stability for shear failure is calculated using Equation 4, where C is the fault cohesive strengh.

$Fs = \sigma_n + (C-\tau)/\mu$ Equation 4

Equation 4 provides the change in pressure required to induce failure of a plane, with lower values indicating higher risks for fault reactivation.

4. Structural framework of the East Irish Sea Basin

Characterisation of the fault network in the EISB was achieved through detailed mapping of geological structures observed in the 3D seismic data (Figures 3 and 5). Figure 5 shows the 3D model with the faults mapped in the study area, shown as grey-coloured surfaces. The fault population consists of two main families, corresponding to the Northern and Southern structural domains identified in the basin by Jackson and Mulholland (1993). The orientation data of the mesh surfaces fitted to the fault geometry are plotted as poles-to-planes on the stereographic plots. The high-density data clouds observed in both structural domains indicate a general bimodal distribution of fault dip directions towards the East and West quadrants.

There are differences in fault trends between the structural domains. Eighty-five faults were mapped in the Northern domain, which are represented as 4258 mesh points in the fault model. The poles indicate a predominantly NW-SE fault orientation, and this trend is clearly discernible on the 3D image. Numerous additional poles plot close to the northern and southern limits of the stereonets. These represent steep, East-West oriented faults that are present in smaller numbers in the basin. The dip frequencies observed show a high range. Although the highest frequencies correspond to fault segments dipping between 40 and 50 degrees, fairly high numbers also occur for values between 30 and 70 degrees. This is due to the presence of very large listric faults in the northern domain, which have curved profiles and have low dip values towards their base (Figure 3a and 3B). The faults mapped in the southern domain have a more constrained range of dip values, with the highest frequencies around 50 to 60 degrees, and there is a clearly marked North-South fault strike trend. This is a direct consequence of the difference in structural styles in this domain, where faults are more numerous and have planar geometries (Figure 3c). Although few East-West faults were identified on the seismic data, such faults may occur, however the data quality precludes their visualisation.

5. Storage Sites in the East Irish Sea Basin

The CO_2 storage potential of the East Irish Sea Basin is primarily confirmed by the presence of thirteen gas fields discovered since the 1970's hosted in Triassic Ormskirk Sandstone reservoir rocks (Figure 1a). While the basin has entered its mature phase in terms of exploration and production, recent discoveries such as the Rhyl Field (Ward and Baker, 2018) demonstrate further potential in the Triassic play, while Pharaoh et al. (2016) suggested that the Carboniferous may also be potentially prospective. The largest field in the EISB, the South Morecambe Field, is estimated to be able to store 734 Mt of CO_2 following its depletion (Kirk, 2006). The Hamilton field has an estimated storage capacity of 125 Mt (Energy, 2016). Its expected availability for storage following cessation of production, coupled with its proximity to shore and existing pipeline infrastructure, make it a key potential storage site with strategic relevance for planned hydrogen-based gas networks for the western UK. In addition to the gas fields, twenty closures in saline aquifers have been identified in the Ormskirk Sandstone Formation (Figure 1a). This brings the currently estimated CO_2 storage capacity of the East Irish Sea Basin to circa 6.7 Gt (Bentham et al., 2014; Kirk, 2006), with additional storage units potentially present in the Permian Collyhurst Sandstone Formation (Gamboa et al., 2016).

The majority of storage sites in the EISB consist of closures on fault-bounded structural highs in Triassic strata (Kirk, 2006; Williams et al., 2018) (Figure 3). Faults are ubiquitous in the area and play a major role on the delimitation of the majority of the structural traps (Figure 1 and 3). Fault spacing is a crucial control on the areal extent of each storage site. These are markedly larger in the northern domain (Figure 1), with particular relevance within the Keys Basin where the larger potential storage sites have been identified due to the lower density of faulting and relatively limited offsets in this region (Figure 3a). Elsewhere in the Northern domain, deep fault-bounded grabens are preserved with the OSF strata present on structural highs. These grabens are infilled with Triassic mudstones of the Mercia Mudstone Formation, the regional caprock for the OSF reservoir, potentially improving the efficiency of lateral seals (Figure 3b). Structural closures towards the south are markedly smaller due to the abundance of closely-spaced faults in the area (Figure 3c). There is also limited suitability for the presence of Triassic storage sites in this domain due to the basin geometry and evolution, which led to erosion and removal of the Triassic strata (Figure 3c).

6. Fault reactivation risk

The potential storage sites identified in the EISB are generally bounded, or affected by, regional faults (Figures 1 and 3). Assessment of fault reactivation risks associated with CCS operations in the EISB made in this work benefits from previous work that defined the regional stress parameters for the area based on earthquake focal mechanisms and a wealth of wells drilled for hydrocarbon exploration. The latter targeted primarily the Triassic reservoir strata, but several extend deeper to Permian and Carboniferous units (see Baptie, 2010; Fellgett et al., 2018; Kingdon et al., 2016 and Williams et al., 2018). Williams et al. (2018) defined the main stress parameters used for the models in this study, described ahead. The authors used borehole image logs to estimate a mean orientation of 062 degrees for the minimum horizontal stress (S_{hmin}). As the maximum horizontal stress orientation, S_{Hmax}, develops at 90 degrees from S_{hmin}, (Zoback, 2010), an average regional of 152 degrees was obtained for the parameter S_{Hmax}, with an estimated standard deviation of 12 degrees. Pressure data inputs derived from the estimation of a consistent pore pressure gradient of 11.62 MPa/km for the Triassic and Permian strata (Williams et al., 2018).

Williams et al. (2018) estimated the magnitude of the vertical stress (S_V) by integrating bulk density logs from 35 individual wells, which can be approximated for the region using a power law function such that:

$$S_V = 0.0159Z^{1.0511} \qquad \text{Equation 5}$$

The published stress model for the EISB estimated a regional gradient of 18 MPa/km for the minimum horizontal stress (S_{hmin}) from pressure leak-off tests from exploration wells. It presented two case scenarios S_{Hmax} gradients, each constrained using Equation 2 and frictional limits μ of 0.6 and 04. In thus study we opted to use the scenario with the higher μ of 0.6, the value beyond which faulting is expected to occur (Reynolds et al 2003). This produces an estimated S_{Hmax} gradient of 31.54 MPa/km, a conservative maximum value, as the higher the differential stress (S_{Hmax} - S_{hmin}) the closer the conditions to failure. The pressure profile gradients used here to assess the fault reactivation in the EISB are summarised in Figure 6.

The response of the 3D fault network to the stress parameters described above was modelled to assess spatial variation in slip tendency and fracture stability (Figure 7 and 8). The stereographic stress representations in figures 7b and 8b show the range of values for both parameters at 800 m, the average depth of the Triassic reservoir targets. The poles associated with the full fault population are shown on these. Additional stereographic projections for the northern and southern domains showing data points limited to the interval between 800 and 1000 m are also included (Figures 7c, 7d, 8c and 8d).

Slip Tendency

The slip tendency analysis indicates that the EISB faults modelled here are stable and have limited risk of reactivation. All fault segments have slip stability values below 0.6, the minimum theoretical value for reactivation, regardless of the domain in which they occur (Figure 9a and 9b). The increase in slip tendency values generally correlate with increased dips on faults, as expected under strike-slip stress regimes. The values close to the theoretical stability limit are those with the highest recorded dips, especially in the southern domain where near-vertical faults occur in higher frequencies. However, there are steep fault sections on the Northern Domain recording slip tendency values below 0.2 despite their higher dip (Figure 9a). The slip tendency on the 3D diagram shows that these low values correspond to faults with a East-West orientation, or segments of the larger faults with similar trends. These strike perpendicularly to the orientation of S_{Hmax} and are affected by higher normal stress (Fig. 7a). In addition, the highest slip tendency values closer to fault reactivation do not have to be specifically associated to particular whole faults but consist of specific segments oriented closer to the optimal reactivation directions (Figure 7a).

Slip tendencies in the Northern Domain generally show lower values, with an average of 0.35, translating into increased fault stability conditions when compared to the Southern one (average of 0.41). This is primarily due to the differences on fault orientation and geometry from both domains under the common regional stress condition. This tendency for stability is particularly relevant at the levels of the main Triassic reservoir units. This is expressed by the data constrained between 800 and 1000 m (Figure 7c), as no fault poles occur close to the poles of the optimal planes of reactivation. The results indicate that 91% of the data show slip tendency values below 0.5, and even if the fault orientation is parallel to the optimal planes of reactivation, their lower dip contributes to the overall stability. A particularly relevant aspect of the low slip tendencies in the Northern domain is that they

occur over large segments of the faults. This is exemplified by predominantly of NW-striking faults, such as the Keys Fault, and the steep East-West striking faults mapped in the 3D seismic data (Figure 7a).

There is an increase in slip tendency in the Southern Domain (Figure 7a and 7d), where 82% of the data points plot below of 0.5. The proximity to slip conditions is indicated by the data clustering surrounding the pole of N-S optimally oriented faults (Figure 7d), to which the majority of faults in the south are sub-parallel (Figure 5). The Mohr diagram further supports this tendency, with numerous points plotting along the circle edge, the latter representing conditions closer to the failure envelope limit (Figure 7d). In contrast, this high frequency of points close to the Mohr envelope is not observed for the diagram of the Northern domain (Figure 7c). The fault pole distribution indicates that east-dipping faults on the Southern domain are generally steeper and have a higher likelihood of reactivation compared to westward-dipping faults. The latter can also show slip tendency values relatively close to the stability limit, but they are predominantly close to or below 0.5 (Figure 7d). Low slip tendency values around 0.2 are also observed for NE-SW fault segments on the Southern domain dipping between 70 and 80 degrees. These do not represent any specific fault, but instead correspond to pronounced localised bends on the geometry of larger N-S faults. An example of this are the southern sections of the Gogarth Fault visualised on the 3D fault diagram (Figure 7), where localised low slip tendency values (blue colours) clearly contrast with the average values along the fault planes (green to yellow colours).

Fracture Stability

The fracture stability results show marked contrasts in their variation patterns when compared to the slip tendency results (Figures 8 and 9). This is mainly due to the introduction of the Pore Pressure gradient to the model. Faults tend to have lower stability values the closer the Pore Pressure gradient is to the main stress gradients (Figure 6). Therefore, faults are less able to withstand higher pressure increases towards their upper sections at shallower depths (Figure 8a). However, the same faults can withstand three or four fold increases of pore pressure towards their base at depth (Figure 8a). The minimum fracture stability to reactivate the weaker faults in the modelled stress conditions is 3.6 MPa (Figure 8). On Mohr diagrams, this corresponds to the pressure required to shift the circle to the limit of the failure envelope (Figure 8c and 8d). The majority of faults do tend to have higher thresholds for pressure increase, but this varies regionally.

Fault in the Northern domain have higher stability, mimicking the trends for the slip tendency results. Faults with lower slip tendencies are able to withstand higher increases in pressure, up to 15 MPa or more, such as the East-West faults and the Keys fault (Figure 8a). Fracture stability reacts to increasing depth and changes to fault geometry (Figure 9c and 9e). For a given depth, steep near-vertical fault segments show the lower values and stability gradually increasing as faults flatten. The minimum is never lower than 3.6-4 MPa, but the maximum can easily exceed 20 MPa. However, there are exceptions to this trend where steep East-West faults show some of the highest fracture stability values (Figure 9c and 9e). These East-West faults are particularly relevant at the Triassic reservoir level (800-1000 m), capable of withstanding up to 19 MPa of overpressure. However, the majority of the faults are considered to be capable of withstanding pressure increases predominantly between 5 and 9 MPa (Figure 8c and 9c).

Fault stability conditions in the Southern domain are comparatively lower as many are sub-parallel to the optimal reactivation planes (Figure 8d). There is an influence of the fault dip direction on this parameter, with west-dipping fault showing ranges between 4.5 and 8 MPa while for east-dipping ones stability is estimated to be between 3 and 6 MPa. Similar to the slip tendency observations, there are segments along the southern fault planes that show higher stability values. These locally reach fairly shallow areas of the fault surface, as exemplified by green colours plotted on the Gogarth Fault plane (Figure 8a). The average Triassic OSF reservoir depth between the 800-900 m considered for the Northern domain has limited validity in the south as strata of this age are often eroded and thus absent (Figure 3C). Instead, the reservoir level in the south is at depths of around 1000 m and limited to areas east of the Gogarth fault (Figures 3c and 8a). Stability conditions at those depths can be more suitable, with values in excess of 10-12 MPa being common (Figure 9d and 9f). The fracture stability plot also shows a wide point dispersion towards high values at depths of between 1000 and 2000 m (Figure 9d and 9f). These correspond to fault segments with dip angles between 60 and 75 degrees and strikes sub-parallel to S_{HMax} mapped at such depths.

7. Discussion

7.1 Suitability and safety of the East Irish Sea Basin for safe CO_2 storage

The storage integrity of CCS sites is dependent on a variety of factors that have to be known prior to, during and after the injection of CO_2, of which caprock integrity and lithology, subsurface pressure and complexity of faults play a major role. The suitability of the caprocks and the risk of leakage through faults are critical to safe and secure CO_2 storage (Nelson et al., 2005; Nicol et al., 2017). Integration of well data with structural models derived from 3D seismic data is critical to producing models that more closely resemble the real geological conditions, yet these may still involve a fair degree of uncertainty when data is extrapolated to scarcely-drilled areas.

The safety of storage sites in the East Irish Sea also depends on the stability of the large faults often bounding them. The fault stability assessment indicates that, under a common state of regional stress, fault structures bounding potential storage sites in Triassic reservoir rocks within the Northern domain are likely to withstand higher pressure increases prior to reactivation than ones to the south (Figure 8). This is expressed by higher fracture stability values to the north, often observed on large parts of the fault planes (Figure 7a and 8a). Faults in the Southern domain are theoretically closer to less stable conditions. This is exemplified by the number of planes plotting near the optimal reactivation orientations, especially for East-dipping structures (Figure 7d and 8d). In addition to this, closures in the south covered by the 3D seismic data are smaller due to the higher compartmentalisation imposed by the high number of faults (Figure 3c). The viability of storage in Triassic reservoirs on the Southern domain is also largely dependent of its tectonic evolution. The top of the Sherwood Sandstone Formation is, within the area covered by the 3D data, often truncated or present at depths shallower than 800 m (Figure 3c), thus compromising the preservation of CO_2 in supercritical state. Storage conditions in this domain are favourable to areas east of the Gogarth Fault where Triassic strata are buried more deeply. Importantly, this includes the Hamilton field, the largest hydrocarbon reservoir towards the south of the EISB bound by North-South faults (Bunce, 2018; Yaliz and Taylor, 2003) and possibly the first CCS site in the area. However,

the lack of seismic data available to this study covering that particular area of the basin prevents us from assessing the fault stability conditions, despite their proven capacity to retain fluids.

7.2 Considerations on regional modelling uncertainty

Understanding of the fault reactivation risk in the EISB has clearly benefitted from detailed mapping, at a 3D seismic scale, of the major fault geometries in three-dimensions. This has highlighted the variability in slip risk and stability that occurs as a function of the fault morphology. The least stable conditions are represented by the fault planes with optimal orientation for reactivation, which are sub-vertical and exhibit the highest slip tendency values obtained (Figure 7b). Such steep faults therefore pose a higher slip risk, as expected for basins under strike-slip stress conditions, and the slip tendency values would be even higher for true vertical planes. The use of 3D seismic-constrained fault surfaces in this study indicates that stable conditions are expected for faults on the EISB at depths relevant to CCS (Figure 9). Despite using the input parameters for *in situ* stress conditions and for fault strength from Williams et al., (2018), the results of this study provide a more robust estimate of fault stability conditions. This model suggests increased fault stability conditions for the EISB in comparison to the earlier work of Williams et al. (2018), demonstrating the additional value gained from integration of accurately constrained fault geometries in 3D models.

There are, however, model uncertainties and limitations that can affect the result. The faults mapped in the EISB show dip values in the order of 50 to 60 degrees (Figure 5), and the stability conditions associated with them clearly shows the relevance of fault geometry on reactivation risk. The fault dip was obtained from a regional depth conversion model derived from borehole sonic logs and check-shot data, but velocity variations can occur laterally as a function of changes in rock density. This has been a recognised issue in the EISB, affecting the visualisation of both reservoir and overburden sequences (Ward and Baker, 2018). Poorly constrained velocity models could lead to different fault dips from the ones measured, affecting the normal and tangential stresses calculated.

The stress conditions, and consequently the model outputs, can also change in space and time. For instance, the orientation of S_{Hmax} has been recognised as a most critical uncertainty affecting fault reactivation (Chiaramonte et al., 2015). A rotation of the orientation of S_{Hmax} in the East Irish Sea Basin was reported by Williams et al. (2018) (see their Figure 6). It consists of a shift of the maximum horizontal stress from a clear NW-SE orientation towards a marked North-South orientation in the southeastern limits of the basin. Despite the latter orientation not being applicable to the study area, there may be shifts from the average orientation of 152 degrees here used within the two main structural domains. To assess the impact of shifts in S_{Hmax} on fracture stability, we calculated the difference in fracture stability (ΔFs) for two scenarios based on the average orientation of N152 plus and minus a standard deviation of circa 12 degrees (Williams et al. 2018). For the northern domain this was calculated as the difference of FS values calculated for S_{Hmax} of N152 and of N140 (Figure 10a). For the southern domain this was calculated for the orientations of N152 and N164 (Figure 10b). Regardless of the domain, the vast majority of data points indicate that the effect of the rotation of S_{Hmax} on ΔFs is limited, predominantly in the order of 1-2 MPa (Figure 10). This is predominantly the case between 800 m to 1000 m on the Northern Domain, at the depth of the larger Triassic age closures (Figures 1a, 3a and 3b). Such ΔFs caused by different orientation of the maximum horizontal stress can be considered to be of low impact as the FS values

obtained are predominantly between 5 and 10 MPa (Figure 9). On the southern domain, where the stress rotation scenario could bring S_{HMax} closer to a North-South orientation (Williams et al., 2018), there is a steadier increase of ΔFs values. This reflects the local effects of fault plane irregularity on the predominantly North-South fault orientation (Figure 5 and 8a). Despite this, the same considerations for the northern faults is applicable to the southern faults, i.e. there is a limited risk that shifts on S_{Hmax} within the study area will decrease the modelled fracture stability towards reactivation conditions.

The stress models provide a good proxy for fault stability and provide an indicator of of how much fluid can be injected before the threshold at the reservoir-bounding faults is reached (Streit and Hillis, 2004). However, the structures may actually be able to withstand higher pressures than those here modelled. This may happen due to poroelastic effects that, in general, this translates into increasing pressure perturbations at locations (or faults) away from the boreholes as CO_2 injection proceeds. Adequate estimates of pressure changes on lateral heterogeneous strata are challenging. These ideally require adequate modelling accounting for pressure changes during injection (e.g. Rutqvist et al., 2007; Williams et al., 2017) and are not achievable through the static models here shown. However, scenarios can be obtained from ΔP_p estimates that reproduce reasonable far-field stress perturbations (Chiaramonte et al., 2015; Jin et al., 2012; Williams et al., 2016). Chiaramonte et al. (2015) determined that a ΔP_p of 10 MPa could either have a limited effect on the reactivation of faults at the Snøhvit field or make them up to 20% more stable. Similarly, Williams et al. (2016) observed an increase in fault stability in the Captain Sandstone aquifer under strike-slip stress regimes due to poroelastic effects of circa 3 MPa. Such is indeed relevant for the stress state of faults on the EISB but would be limited on the regional scale here presented. It will, however, be of relevance for future work that assesses in detail the stability and pressure retention capacity faults delimiting the main CCS sites planned for the EISB, namely the Hamilton and Morecambe fields.

Smaller scale parameters such as the geotechnical properties of the fault gouge and the fault damage zones (Mitchell and Faulkner, 2012; Riley et al., 2010; Takahashi, 2003) influence fault stability but such factors that cannot be determined from seismic data alone. These features will influence the value of fault rock cohesion input to the model, and consequently their stability output. Despite our use of a cohesion value of 2MPa, several studies tend to use scenarios of zero cohesion for fault reactivation (e.g., Chiaramonte et al., 2015; Rutqvist et al., 2007; Williams et al., 2016), which indicate the lower limiting boundary for overpressure (Sibson, 2003). A zero-cohesion input would effectively decrease the failure envelope on our data by a value of circa 3 MPa. This brings fault planes that plot close to the limit of the Mohr circle very close to reactivation conditions and only able to withstand limited pressurisation (Fig. 11). However, it is licit to expect some level of cohesion of faults at depth due to increases in normal stress (Byerllee, 1978), or gouge strengthening by cementation or mineral growth (Cappa and Rutqvist, 2011; Giger et al., 2008). The latter can be particularly relevant on the EISB given the occurrence of a strata-cutting ilite cementation level that affects the Triassic reservoirs (Knipe et al., 1993). Obtaining accurate cohesion values from fault samples at depth is challenging thus models rely on estimations, hence our use of 2 MPa for this parameter. However, this is still the within range and more conservative than fault cohesion values considered in modelled scenarios for CCS sites offshore Norway (Chiaramonte et al., 2015; Skurtveit et al., 2018).

Despite these uncertain variables, crucial for local reservoir evaluation, early-stage assessments of regional-scale leakage risks associated with CCS are achievable by integrating in situ stress and 3D geological models. The techniques described here are applicable in onshore and offshore sedimentary basins considered for CO_2 sequestration.

8. Conclusions

The fault stress model presented here provide an insight into the stability of fault structures in the East Irish Sea Basin, with the specific aim to assess their stability during the injection and storage of CO_2. The mapping of the fault geometry on 3D seismic data and the modelling of their stability leads to the following conclusions:

- Two main structural trends have been identified within the area covered by the seismic data, corresponding to a Northern and Southern domain.
- Faults in the Northern domain predominantly follow a NW-SE orientation, complemented by sub-perpendicular faults with general E-W orientations. Fault dips in the order of 30 to 40 degrees are common at depth due to the listric geometry of large graben-bounding faults.
- Faults in the Southern domain have a predominantly N-S strike orientation, are more numerous, and generally steeper. Faults with E-W orientations have not been clearly identified in this domain, but this may be due to limitations in the resolution of the seismic.
- The faults interpreted from the seismic data formed the framework to evaluate the effect of 3D geometry on their reactivation potential based on the regional fault stress model from Williams et al. (2018). This considered a strike-slip regime, with a sub-horizontal maximum stress component oriented at N152.
- Calculations of the fault Slip Tendency indicate that, under current conditions, there is a limited risk of fault reactivation. All values calculated fall below 0.6, the value for the onset of slip, regardless of the structural domain and fault geometry.
- The Fracture Stability attribute returns an indicator of how much pressure a fault can withstand prior to rupture, depending on their dip and orientation. In our model, minimum stability values generally exceed 3 MPa at the Triassic reservoir level. The highest values are observed along faults sub-perpendicular to N152, the orientation of maximum horizontal stress.
- As variations in stress orientation occur within the basin, we estimated the impact of rotation of the maximum horizontal stress on fracture stability. The variations in horizontal stress orientation have limited effect on the fracture stability, generally within 1 or 2 MPa. These values do not immediately compromise the fault stability obtained from the stress modelling.
- Detailed evaluation of pressure build-up and propagation affects, including the impact of fault compartmentalisation, should be conducted during assessment of specific sites for CO_2 storage, to ensure that fault reactivation will not compromise storage integrity.
- This work demonstrates the additional value gained from the integration of accurately constrained fault geometries in 3D stress models.

The preferential storage sites are located on the Northern domain where larger closures occur and faults have a higher stability. However, stable closures may be present within the Southern domain,

especially to the East of the study area, but there was no data available to confirm this. This work highlights the strategic importance of the EISB for CCS in the western UK. This has gained further strategic relevance with the planned implementation of hydrogen networks in the western UK, which include plans to use carbon storage sites on the East Irish Sea Basin.

Acknowledgements

Funding to support this research was provided by Welsh Government and HEFCW through Ser Cymru National Research Network for Low Carbon, Energy and the Environment (NRN-LCEE) via Geo-Carb-Cymru Cluster (ACM, DS, MB). CO2Stored data is © The Energy Technologies Institute LLP, NERC and The Crown Estate. All rights reserved. The bathymetric metadata and Digital Terrain Model data products have been derived from the EMODnet Bathymetry portal - http://www.emodnet-bathymetry.eu. DG, JDOW, MB and DIS publish with the permission of the Executive Director, British Geological Survey. Gareth Williams is acknowledged for comments and discussions on this work. The authors would like to thank the editor and two anonymous reviewers for the constructive comments provided.

References

Addis, M.A., Hanssen, T.H., Yassir, N., Willoughby, D.R., Enever, J., 1998. Comparison of leak-off test and extended leak-off test data for stress estimation, Proceedings of the SPE/ISRM Rock Mechanics in Petroleum Engineering Conference, pp. 131-140.

Aydin, A., 2000. Fractures, faults, and hydrocarbon entrapment, migration and flow. Marine and Petroleum Geology 17, 797-814.

Azar, C., Lindgren, K., Obersteiner, M., Riahi, K., van Vuuren, D.P., den Elzen, K.M.G., Möllersten, K., Larson, E.D., 2010. The feasibility of low CO 2 concentration targets and the role of bio-energy with carbon capture and storage (BECCS). Climatic Change 100, 195-202.

Bachu, S., 2015. Review of CO2 storage efficiency in deep saline aquifers. International Journal of Greenhouse Gas Control 40, 1-15.

Bachu, S., Bonijoly, D., Bradshaw, J., Burruss, R., Holloway, S., Christensen, N.P., Mathiassen, O.M., 2007. CO2 storage capacity estimation: Methodology and gaps. International Journal of Greenhouse Gas Control 1, 430-443.

Bachu, S., Grobe, M., 2006. Characterization of sites for geological storage of carbon dioxide. Environmental Geosciences 13, 67-70.

Backe, G., Holford, S.P., Tenthorey, E., Mitchell, A., 2015. 3D seismic analysis of complex faulting patterns above the Snapper Field, Gippsland Basin: implications for CO2 storage AU - Swierczek, E. Australian Journal of Earth Sciences 62, 77-94.

Baines, S.J., Worden, R.H., 2004. Geological Sequestration of Carbon Dioxide. Geological Society, London, Special Publications 233.

Baptie, B., 2010. Seismogenesis and state of stress in the UK. Tectonophysics 482, 150-159.

Barton, C.A., Zoback, M.D., Moos, D., 1995. Fluid flow along potentially active faults in crystalline rock. Geology 23, 683-686.

Bastin, J.C., Boycott-Brown, T., Sims, A., Woodhouse, R., 2003. The South Morecambe Gas Field, Blocks l10/2a, l10/3a, l10/7a and l10/8a, East Irish Sea, in: Gluyas, J.G., Hichens, H.M. (Eds.), United Kingdom Oil and Gas Fields, Commemorative Millennium Volume. Geological Society, London, Memoir, 20, pp. 107-118.

Benson, S.M., Cole, D.R., 2008. CO2 Sequestration in Deep Sedimentary Formations. Elements 4, 325-331.

Bentham, M., Kirby, M., 2005. CO2 storage in saline aquifers. Oil & gas science and technology 60, 559-567.

Bentham, M., Mallows, T., Lowndes, J., Green, A., 2014. CO2 STORage Evaluation Database (CO2 Stored). The UK's online storage atlas. Energy Procedia 63, 5103-5113.

Bradshaw, J., Cook, P., 2001. Geological Sequestration of Carbon Dioxide. Environmental Geosciences 8, 149-151.

Breckels, I.M., van Eekelen, H.A.M., 1982. Relationship Between Horizontal Stress and Depth in Sedimentary Basins. SPE-10336-PA 34, 2191-2199.

Bretan, P., Yielding, G., Mathiassen, O.M., Thorsnes, T., 2011. Fault-seal analysis for CO2 storage: an example from the Troll area, Norwegian Continental Shelf. Petroleum Geoscience 17, 181-192.

Bunce, J., 2018. The history of exploration and development of the Liverpool Bay fields and the East Irish Sea Basin, in: Craig, J., Gerali, F., MacAulay, F., Sorkhabi, R. (Eds.), History of the European Oil and Gas Industry. Geological Society, London, Special Publications.

Byerlee, J.D., 1978. Friction of rocks. Pure Appl. Geophys. 116, 615–626.

Cartwright, J., Huuse, M., Aplin, A., 2007. Seal bypass systems. AAPG Bulletin 91, 1141-1166.

Cappa, F., Rutqvist, J., 2011. Modeling of coupled deformation and permeability evolution during fault reactivation induced by deep underground injection of CO2. International Journal of Greenhouse Gas Control, 5(2), 336-346.

Chadwick, A., Arts, R., Bernstone, C., May, F., Thibeau, S., Zweigel, P., 2006. Best practice for the storage of CO 2 in saline aquifers. 1-289.

Chadwick, R.A., Kirby, G.A., Baily, H.E., 1994. The post-Triassie structural evolution of north-west England and adjacent parts of the East Irish Sea. Proceedings of the Yorkshire Geological Society 50, 91-102.

Chiaramonte, L., Zoback, M.D., Friedmann, J., Stamp, V., 2008. Seal integrity and feasibility of CO2 sequestration in the Teapot Dome EOR pilot: geomechanical site characterization. Environmental Geology 54, 1667-1675.

Chiaramonte, L., White, J. A., Trainor-Guitton W., 2015. Probabilistic geomechanical analysis of compartmentalization at the Snøhvit CO2 sequestration project. Journal of Geophysical Research: Solid Earth 120.2, 1195-1209.

Colter, V.S., 1997. The East Irish Sea Basin - from caterpillar to butterfly, a thirty-year metamorphosis, in: Meadows, N.S., Trueblood, S.P., Hardman, M., Cowan, G. (Eds.), Petroleum Geology of the Irish Sea and Adjacent Areas. Geological Society Special Publication No. 124, pp. 1-9.

Damen, K., van Troost, M., Faaij, A., Turkenburg, W., 2007. A comparison of electricity and hydrogen production systems with CO2 capture and storage—Part B: Chain analysis of promising CCS options. Progress in Energy and Combustion Science 33, 580-609.

Dodds, P.E., Demoullin, S., 2013. Conversion of the UK gas system to transport hydrogen. international journal of hydrogen energy 38, 7189-7200.

Energy, P.B.D., 2016. A Summary of Results from the Strategic UK CO_2 Storage Appraisal Project.

Engelder, T., 1993. Stress regimes in the lithosphere. Princeton, New Jersey, Princeton.

Fellgett, M.W., Kingdon, A., Williams, J.D.O., Gent, C.M.A., 2018. Stress magnitudes across UK regions: New analysis and legacy data across potentially prospective unconventional resource areas. Marine and Petroleum Geology 97, 24-31.

Ferrill, D.A., Morris, A.P., 2002. Dilational normal faults. Journal of Structural Geology 25, 183-196.

Ferrill, D.A., Morris, A.P., McGinnis, R.N., Smart, K.J., Wigginton, S.S., Hill, N.J., 2017. Mechanical stratigraphy and normal faulting. Journal of Structural Geology 94, 275-302.

Firoozabadi, A., Cheng, P., 2010. Prospects for subsurface CO2 sequestration. AIChE Journal 56, 1398-1405.

Gamboa, D., Williams, J.D., Kirk, K., Gent, C.M., Bentham, M., Schofield, D.I., 2016. The Collyhurst Sandstone as a secondary storage unit for CCS in the East Irish Sea Basin (UK), AGU Fall Meeting Abstracts.

Gibbins, J., Chalmers, H., 2008. Carbon capture and storage. Energy Policy 36, 4317-4322.

Giger, S. B., Cox, S. F., Tenthorey, E., 2008. Slip localization and fault weakening as a consequence of fault gouge strengthening—Insights from laboratory experiments. Earth and Planetary Science Letters, 276(1-2), 73-84.

Gough, C., Upham, P., 2011. Biomass energy with carbon capture and storage (BECCS or Bio-CCS). Greenhouse Gases: Science and Technology 1, 324-334.

Haig, D., Pickering, S., Probert, R., 1997. The Lennox oil and gas field, in: Meadows, N.S., Trueblood, S.P., Hardman, M., Cowan, G. (Eds.), Petroleum Geology of the Irish Sea and Adjacent Areas. Geological Society Special Publication No. 124, pp. 417-436.

Halland, E.K., Riis, F., Magnus, C., Johansen, W.T., Tappel, I.M., Gjeldvik, I.T., Solbakk, T., Pham, V.T.H., 2013. CO2 Storage Atlas of the Norwegian Part of the North Sea. Energy Procedia 37, 4919-4926.

Haszeldine, R.S., 2009. Carbon capture and storage: how green can black be? Science 325, 1647-1652.

Hillis, R.R., Gatliff, R.W., Stoker, M.S., Turner, J.P., 2008. Cenozoic exhumation of the southern British Isles. Geology 36, 371-374.

Holford, S.P., Turner, J.P., Green, P.F., Hillis, R.R., 2009. Signature of cryptic sedimentary basin inversion revealed by shale compaction data in the Irish Sea , western British Isles. Tectonics 28.

IEAGHG, 2011. Caprock Systems for CO_2 Geological Storage, 2011/01, June, 2011.

IEAGHG, 2016. Fault Permeability, 2016/13, October, 2016.

IEAGHG, 2017a. CCS deployment in the context of regional developments in meeting long-term climate change objectives.

IEAGHG, 2017b. CO_2 Migration in the Overburden, 2017/08, August, 2017.

IPCC, 2011. IPCC Special Report on Carbon Dioxide Capture and Storage. Environmental Science and Technology 45, 5710-5716.

Jackson, D.I., Jackson, A.A., Evans, D., Wingfield, R.T.R., Barnes, R.P., Arthur, M.J., 1995. United Kingdom Offshore Regional Report: The geology of the Irish Sea.

Jackson, D.I., Johnson, H., Smith, N.J.P., 1997. Stratigraphical relationships and a revised lithostratigraphical nomenclature for the Carboniferous, Permian and Triassic rocks of the offshore East Irish Sea Basin, in: Meadows, N.S., Trueblood, S.P., Hardman, M., Cowan, G. (Eds.), Petroleum Geology of the Irish Sea and Adjacent Areas. Geological Society Special Publication No. 124, pp. 11-32.

Jackson, D.I., Mulholland, P., 1993. Tectonic and stratigraphic aspects of the East Irish Sea Basin and adjacent areas: contrasts in their post-Carboniferous structural styles, in: Parker, J.R. (Ed.), Petroleum Geology of Northwest Europe: Proceedings of the 4th Conference. Geological Society, London, pp. 791-808.

Jin, M., Mackay, E., Quinn, M., Hitchen, K., Akhurst, M., 2012. Evaluation of the CO2 storage capacity of the Captain Sandstone Formation. Paper SPE 154539 presented at the EAGE/SPE Europec Conference and Exhibition, Copenhagen, Denmark, 4–7 June 2012.

Kingdon, A., Fellgett, M.W., Williams, J.D.O., 2016. Use of borehole imaging to improve understanding of the in-situ stress orientation of Central and Northern England and its implications for unconventional hydrocarbon resources. Marine and Petroleum Geology 73, 1-20.

Kirk, K., 2006. Potential for storage of carbon dioxide in the rocks beneath the East Irish Sea.

Knipe, R.J., Cowan, G., Balendran, V.S., 1993. The tectonic history of the East Irish Sea Basin with reference to the Morecambe Fields, in: Parker, J.R. (Ed.), Petroleum Geology of Northwest Europe: Proceedings of the 4th Conf. The Geological Society, London, pp. 857-866.

Li, Z., Dong, M., Li, S., Huang, S., 2006. CO2 sequestration in depleted oil and gas reservoirs—caprock characterization and storage capacity. Energy Conversion and Management 47, 1372-1382.

Lisle, R.J., Srivastava, D.C., 2004. Test of the frictional reactivation theory for faults and validity of fault-slip analysis. Geology 32, 569-572.

Maia, A.R., Cartwright, J., Andersen, E., 2016. Shallow plumbing systems inferred from spatial analysis of pockmark arrays. Marine and Petroleum Geology 77, 865-881.

Marbán, G., Valdés-Solís, T., 2007. Towards the hydrogen economy? International Journal of Hydrogen Energy 32, 1625-1637.

Mazzoldi, A., Rinaldi, A.P., Borgia, A., Rutqvist, J., 2012. Induced seismicity within geological carbon sequestration projects: Maximum earthquake magnitude and leakage potential from undetected faults. International Journal of Greenhouse Gas Control 10, 434-442.

Mcfarland, J.M., Morris, A.P., Ferrill, D.A., 2012. Stress inversion using slip tendency. Computers and Geosciences 41, 40-46.

Mitchell, T.M., Faulkner, D.R., 2012. Towards quantifying the matrix permeability of fault damage zones in low porosity rocks. Earth and Planetary Science Letters 339-340, 24-31.

Morris, A., Ferrill, D.A., Henderson, D.B., Morris, A., Ferrill, D.A., Henderson, D.B., 1996. Slip-tendency analysis and fault reactivation. Geology, 275-278.

Needham, T.I.M., Morgan, R., 1997. The East Irish Sea and adjacent basins : new faults or old ? Journal of the Geological Society 154, 145-150.

Nelson, C.R., Evans, J.M., Sorensen, J.A., Steadman, E.N., Harju, J.A., 2005. Factors affecting the potential for CO2 leakage from geologic sinks, pp. 1-36.

Nicol, A., Seebeck, H., Field, B., McNamara, D., Childs, C., Craig, J., Rolland, A., 2017. Fault permeability and CO2 storage. Energy Procedia 114, 3229-3236.

Petrie, E.S., Evans, J.P., Bauer, S.J., 2014. Failure of cap-rock seals as determined from mechanical stratigraphy, stress history, and tensile-failure analysis of exhumed analogs. AAPG Bulletin 98, 2365-2389.

Pharaoh, T.C., Smith, N.J.P., Kirk, K., Kimbell, G.S., Gent, C., Quinn, M., Monaghan, A.A., 2016. Palaeozoic Petroleum Systems of the Irish Sea Energy and Marine Geoscience Programme. British Geological Survey Commissioned Report CR/16/045, 135.

Reynolds, C.A., Blunt, M.J., Krevor, S., 2018. Multiphase Flow Characteristics of Heterogeneous Rocks From CO 2 Storage Reservoirs in the United Kingdom. Water Resources Research 54, 729-745.

Riley, P.R., Goodwin, L.B., Lewis, C.J., 2010. Controls on fault damage zone width, structure, and symmetry in the Bandelier Tuff, New Mexico. Journal of Structural Geology 32, 766-780.

RISCS, 2014. A Guide to potential impacts of CO_2 storage, in: Pearce, J., Blackford, J., Beaubien, S., Foekema, E., Gemeni, V., Gwosdz, S., Jones, D., Kirk, K., Lions, J., Metcalfe, R., Moni, C., Smith, K., Steven, M., West, J., Ziogou, F. (Eds.), British Geological Survey.

Roberts, J.J., Wilkinson, M., Naylor, M., Shipton, Z.K., Wood, R.A., Haszeldine, R.S., 2017. Natural CO2 sites in Italy show the importance of overburden geopressure, fractures and faults for CO2 storage performance and risk management, in: Turner, J.P., Healy, D., Hillis, R.R., Welch, M.J. (Eds.), Geomechanics and Geology. Geological Society, London, Special Publications, 458.

Rutqvist, J., Birkholzer, J., Cappa, F., Tsang, C. F., 2007. Estimating maximum sustainable injection pressure during geological sequestration of CO2 using coupled fluid flow and geomechanical fault-slip analysis. Energy Conversion and Management, 48(6), 1798-1807.

Schrag, D.P., 2009. Storage of carbon dioxide in offshore sediments. Science 325, 1658-1659.

Sibson, R.H., 1985. A note on fault reactivation. Journal of Structural Geology 7, 751-754.

Sibson, R.H., 1995. Selective fault reactivation during basin inversion: potential for fluid redistribution through fault-valve action, Basin Inversion. Geological Society Special Publication, pp. 3-19.

Sibson, R.H., 1996. Structural permeability of fluid-driven fault-fracture meshes. Journal of Structural Geology 18, 1031-1042.

Sibson, R.H., 2003. Brittle-failure controls on maximum sustainable overpressure in different tectonic regimes. AAPG bulletin 87, 901-908.

Skurtveit, E., Choi, J. C., Osmond, J. L., Mulrooney, M. J., Braathen, A., 2018. 3D fault integrity screening for Smeaheia CO2 injection site. 14th International Conference on Greenhouse Gas Control Technologies, GHGT-14, 21st -25th October 2018, Melbourne, Australia.

Streit, J.E., Hillis, R.R., 2004. Estimating fault stability and sustainable fluid pressures for underground storage of CO2 in porous rock. Energy 29, 1445-1456.

Streit, J.E., Siggins, A.F., Evans, B.J., 2005. Predictine and monitoring geomechanical effects of CO_2 injection, in: Thomas, D.C., Benson, S.M. (Eds.), Carbon Dioxide Capture for Storage in Deep Geologic Formations, Volume 2. Elsevier, pp. 751-766.

Takahashi, M., 2003. Permeability change during experimental fault smearing. Journal of Geophysical Research: Solid Earth 108.

Tiab, D., Donaldson, E.C., 2015. Petrophysics: theory and practice of measuring reservoir rock and fluid transport properties. Gulf professional publishing.

Ward, G., Baker, D., 2018. Rhyl Field: developing a new structural model by integrating basic geological principles with advanced seismic imaging in the Irish Sea, in: Bowman, M., Levell, B. (Eds.), Petroleum Geology of NW Europe: 50 Years of Learning - Proceedings of the 8th Petroleum Geology Conference. Geological Society of London, pp. 355-371.

Williams, J.D.O., Gent, C., Fellgett, M., Gamboa, D., 2018. Impact of in situ stress and fault reactivation on seal integrity in the East Irish Sea Basin, UK. Marine and Petroleum Geology 92, 685-696.

Williams, J.D.O., Fellgett, M.W., Quinn, M.F., 2016. Carbon dioxide storage in the Captain Sandstone aquifer: determination of *in situ* stresses and fault-stability analysis. Petroleum Geoscience, petgeo2016-2036.

Wilson, A.A., 1990. The Mercia Mudstone Group (Trias) of the East Irish Sea Basin. PROCEEDINGS OF THE YORKSHIRE GEOLOGICAL SOCIETY 48, 1-22.

Yaliz, A., Taylor, P., 2003. The Hamilton and Hamilton North Gas Fields, Block l10/13a, East Irish Sea, in: Gluyas, J.G., Hichens, H.M. (Eds.), United Kingdom Oil and Gas Fields, Commemorative Millennium Volum. Geological Society, London, Memoir, 20,, pp. 77-86.

Zoback, M.D., 2010. Reservoir geomechanics. Cambridge University Press.

Figure Captions

Figure 1- a) Regional map showing the study area, highlighting the limits of the Ormskirk Sandstone formation in the subsurface, major fault and structural closures considered for CCS. Closures in red represent depleting hydrocarbon fields, and in green represent saline aquifers. Bathymetric data from EMODnet (http://www.emodnet-bathymetry.eu/). Coastline and hydrocarbon field line work contain public sector information licenced under the Open Government Licence v3.0. b) simplified structural map showing the main fault trends intersecting Triassic strata, identifying relevant basins and faults. Two structural domains are delimited based on fault orientation (modified from Jackson et al., 1995). c) Representative cross-section across the East Irish Sea, highlighting the horst and graben geometry (modified from Jackson et al., 1995).

Figure 2- Stratigraphic column of the East Irish Sea, modified from Williams et al. (2018).

Figure 3- Seismic sections across the East Irish Sea. a) and b) illustrate the structural style in the Northern Domain, where the formation of grabens and half-grabens is controlled by large listric faults detaching on Permian evaporites. c) illustrates the structural style in the Southern Domain, with higher fault frequency and closer spacing. The Sherwood Sandstone Group is often eroded or too shallow for CCS in certain areas towards the south of the EISB. Seismic images shown in a) and b) are derived from the BG943F0001 3D survey, and c) from the CV933F0001 3D survey.

Figure 4- a) Representation of a mapped fault surface as a mesh grid for application in the stress models (top) and representation of the fault mean principal plane, mean pole, and numerous poles of the individualised mesh planes on an equal area projection stereonet (bottom). b) Representation of the normal stress (σn) and shear stress (τ) on a plane affected by an oriented stress vector. c) Diagram showing the shift of a Mohr diagram towards the limit of the failure envelope as an effect of increase in pressure and decrease in effective normal stress.

Figure 5- Three-dimensional depth model representing the fault planes (grey colours) mapped on the 3D seismic data. The two surfaces represent the Top Sherwood Sandstone Group (bronze colours) and the Top Permian (blue colours). Two structural domains are established based on the fault plane geometry.

Figure 6- Regional pressure profile for the East Irish Sea Basin derived from stress parameters in Williams et al. (2018).

Figure 7- a) Three-dimensional representation of changes in Slip Tendency along the fault planes mapped. Slip Tendency values are generally below the estimated onset of slip, especially on the Northern domain. b) Stereographic representation of the Slip Tendency values under the modelled stress conditions, poles of all fault meshes mapped, and optimally-oriented fault planes. c) and d) stereographic projections and Mohr diagrams for Slip Tendency and poles for faults between 800 m and 1000 m depth on the Northern and Southern domains, respectively.

Figure 8- a) Three-dimensional representation of changes in Fracture Stability along the fault planes mapped. b) Stereographic representation of the Fracture Stability values under the modelled stress conditions, poles of all fault meshes mapped, and optimally oriented fault planes. c) and d) represent the stereographic projections and Mohr diagrams for Fracture Stability and poles for faults between 800 m and 1000 m depth on the Northern and Southern domains, respectively.

Figure 9 – Coupled plots for the Northern and Southern structural domains representing the depth versus trend changes in: a) and b) Slip Tendency versus fault dip, c) and d) Fracture Stability versus fault dip, and e) and f) Fracture Stability versus fault strike.

Figure 10 – Plots showing the changes in Fracture Stability values of both domains due to rotation of the maximum horizontal stress vector as a function of depth and fault plane orientation.

Figure 11 - Mohr diagram showing the failure envelope for models with cohesion values of 2 MPa (blue line) and 0 MPa (red line). The latter assumes frictionless faults.

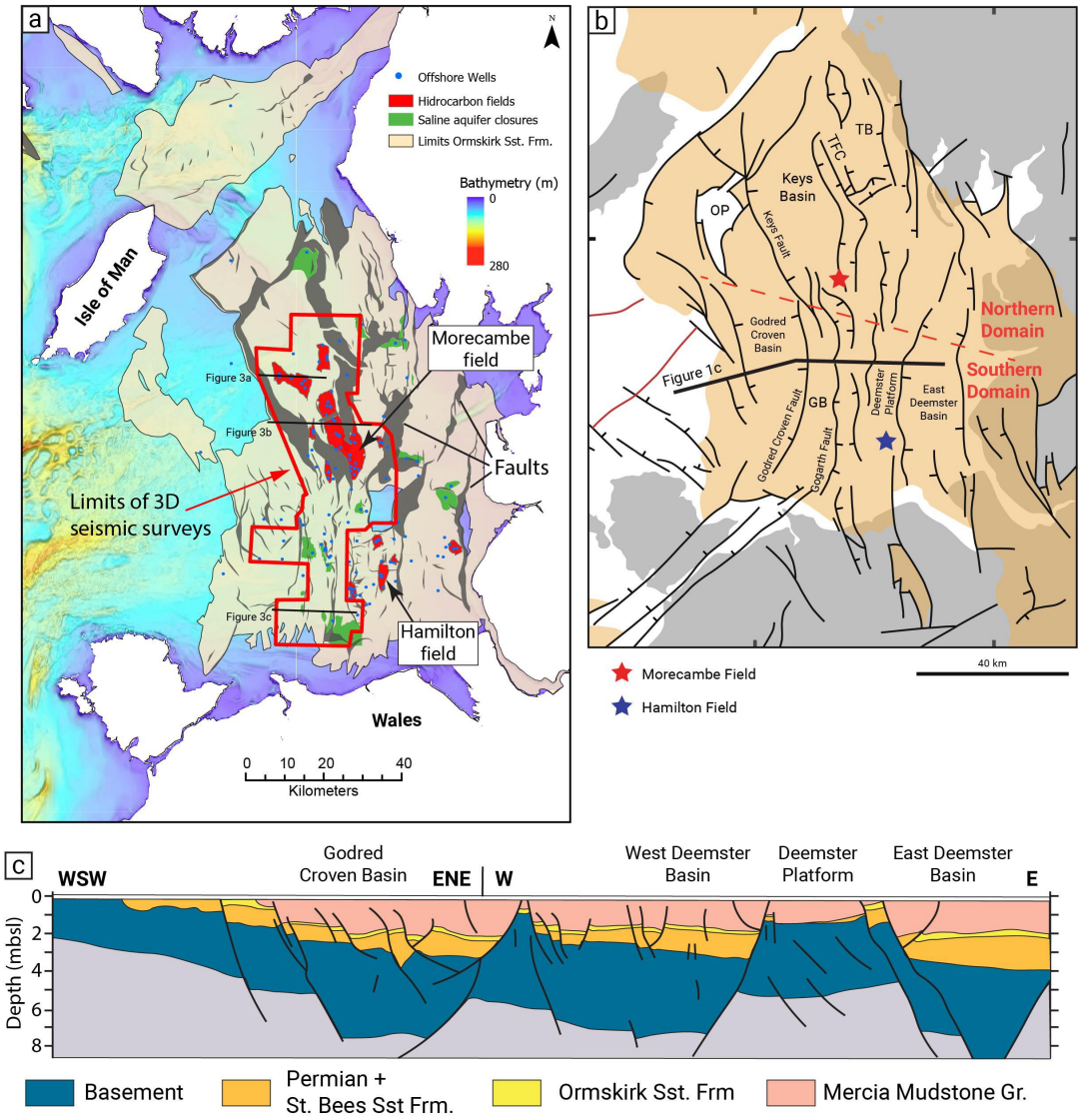
a
N
Offshore Wells
Hidrocarbon fields
Saline aquifer closures
Limits Ormskirk Sst. Frm.
Bathymetry (m)
0
280
Isle of Man
Morecambe field
Figure 3a
Figure 3b
Faults
Limits of 3D seismic surveys
Figure 3c
Hamilton field
Wales
0 10 20 40
Kilometers
b
TB
TFC
Keys Basin
OP
Keys Fault
Godred Croven Basin
Northern Domain
Figure 1c
Southern Domain
GB
Deemster Platform
East Deemster Basin
Godred Croven Fault
Edgarth Fault
40 km
Morecambe Field
Hamilton Field
c
WSW
Godred Croven Basin
ENE
W
West Deemster Basin
Deemster Platform
East Deemster Basin
E
Depth (mbsl)
0
2
4
6
8
Basement
Permian + St. Bees Sst Frm.
Ormskirk Sst. Frm
Mercia Mudstone Gr.

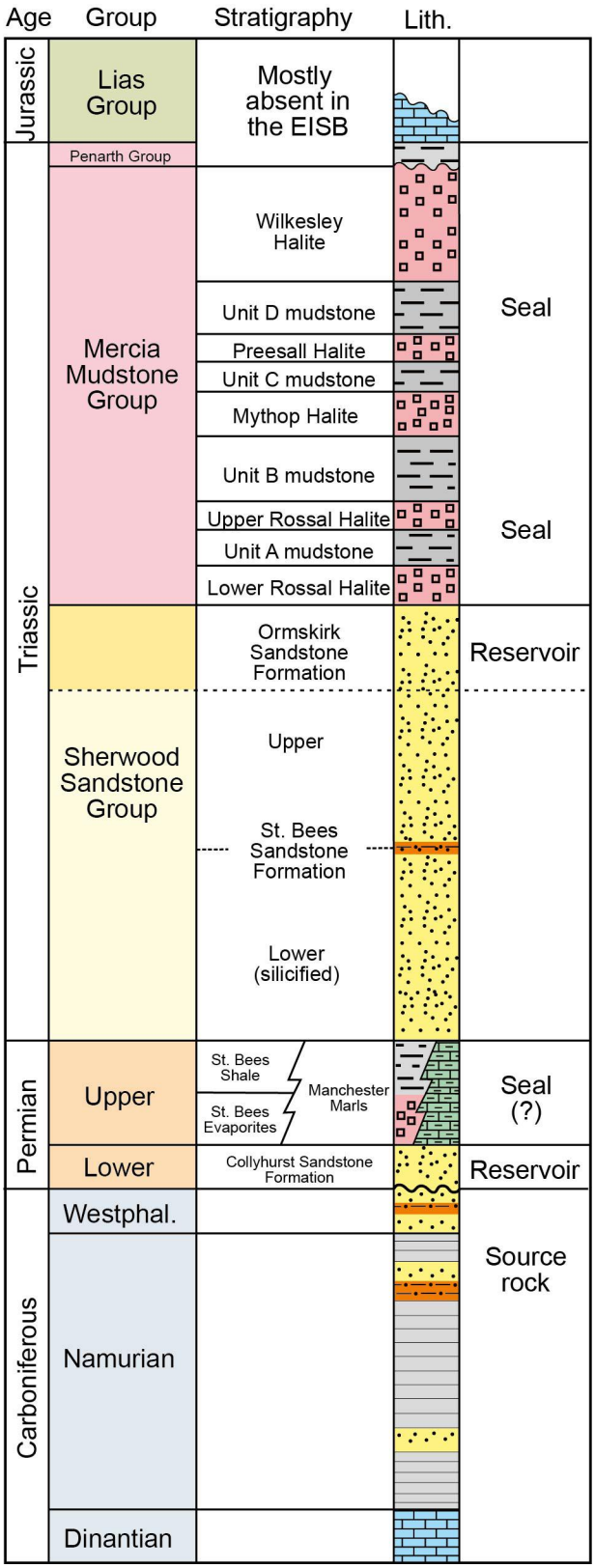
Age
Group
Stratigraphy
Lith.
Jurassic
Lias Group
Mostly absent in the EISB
Penarth Group
Triassic
Mercia Mudstone Group
Wilkesley Halite
Unit D mudstone
Preesall Halite
Unit C mudstone
Mythop Halite
Unit B mudstone
Upper Rossal Halite
Unit A mudstone
Lower Rossal Halite
Seal
Seal
Ormskirk Sandstone Formation
Reservoir
Sherwood Sandstone Group
Upper
St. Bees Sandstone Formation
Lower (silicified)
Permian
Upper
St. Bees Shale
St. Bees Evaporites
Manchester Marls
Seal (?)
Lower
Collyhurst Sandstone Formation
Reservoir
Carboniferous
Westphal.
Namurian
Dinantian
Source rock

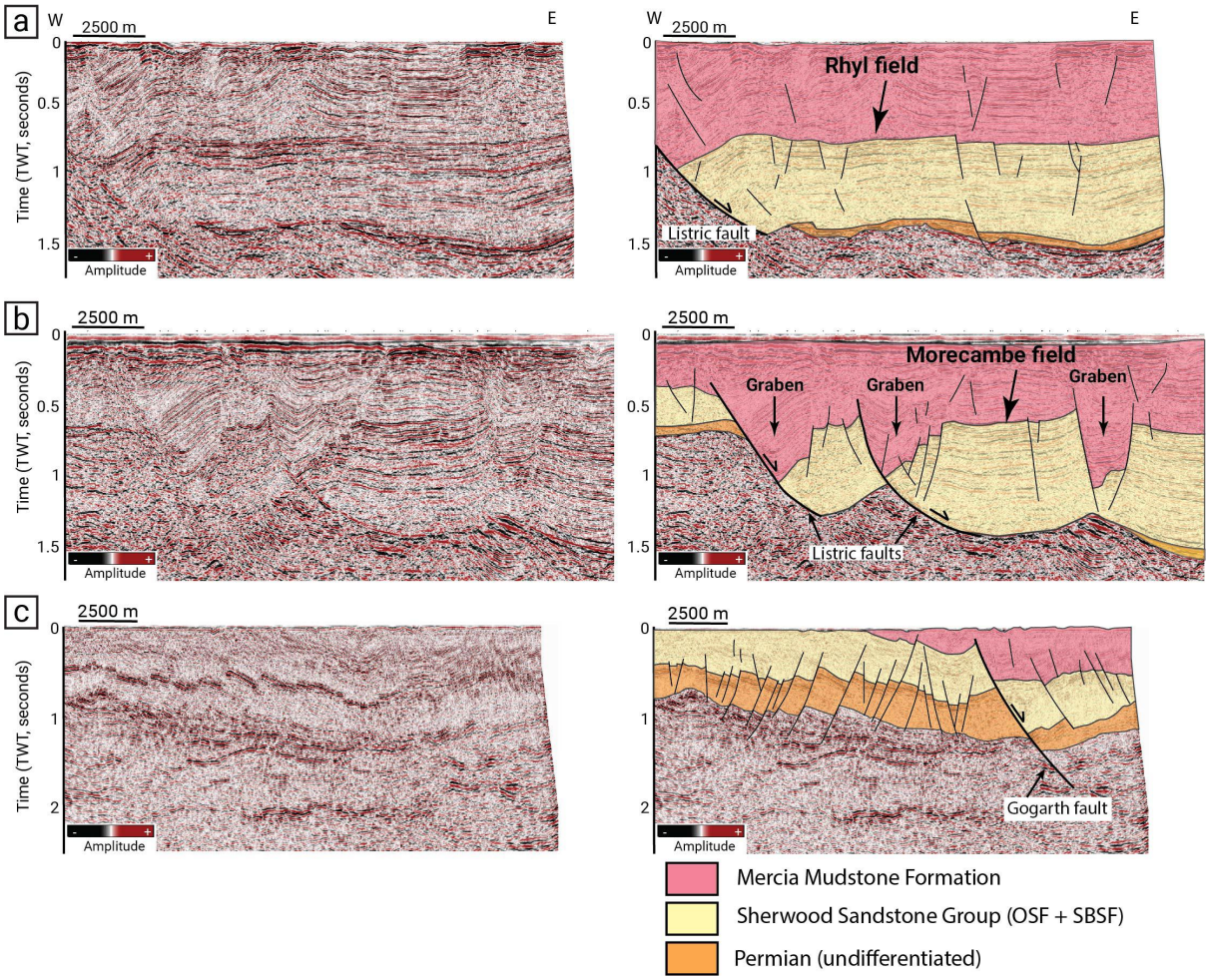
a
W
E
2500 m
Time (TWT, seconds)
0
0.5
1
1.5
Amplitude
Rhyl field
Listric fault
b
Morecambe field
Graben
Graben
Graben
Listric faults
c
2
Gogarth fault
Mercia Mudstone Formation
Sherwood Sandstone Group (OSF + SBSF)
Permian (undifferentiated)

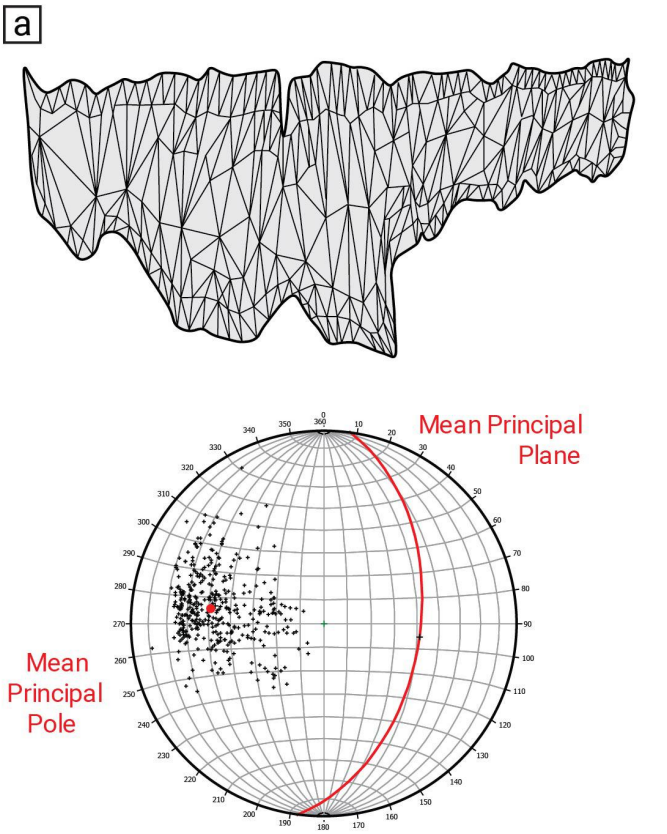
a
Mean Principal Plane
Mean Principal Pole
b
σ1
σ3
σ2
Stress Vector
θ
Normal Stress (σn)
Shear Stress (τ)
c
Shear stress
Mohr failure envelope
ΔP
Effective normal stress

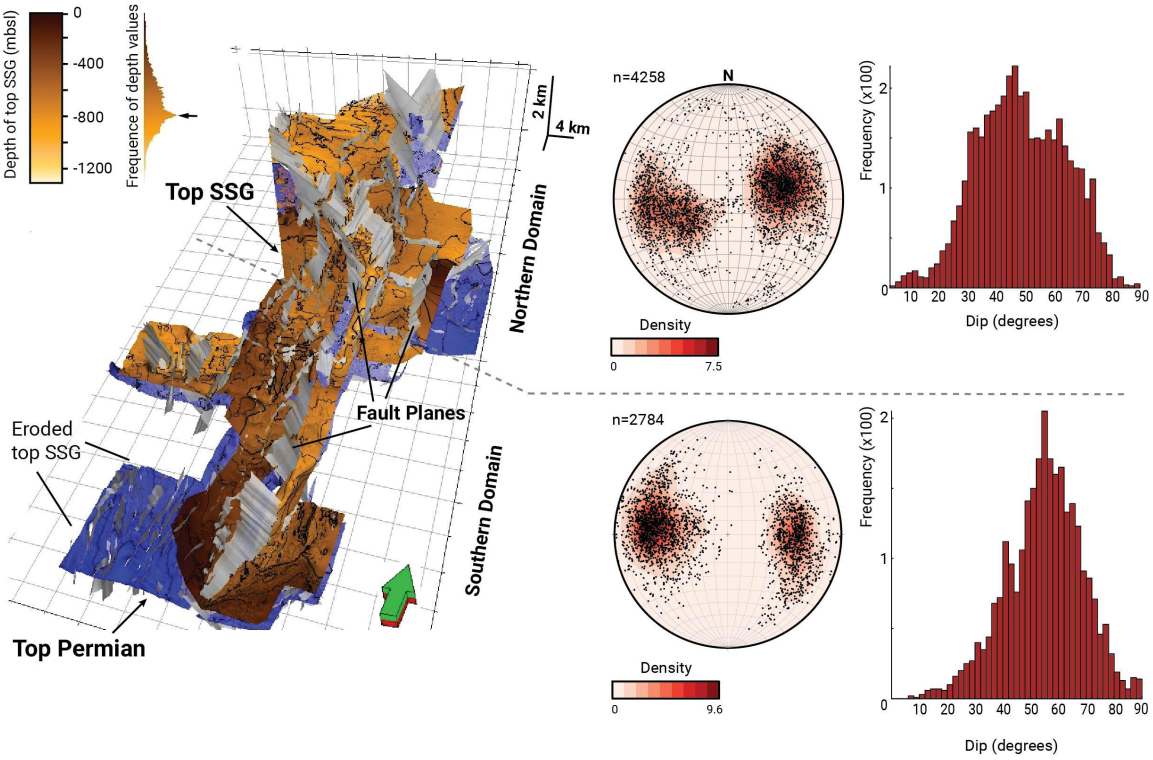
Depth of top SSG (mbsl)
0
-400
-800
-1200
Frequence of depth values
Top SSG
Northern Domain
2 km
4 km
Fault Planes
Eroded
top SSG
Southern Domain
Top Permian
n=4258
N
Density
0
7.5
Frequency (x100)
Dip (degrees)
n=2784
Density
0
9.6
Frequency (x100)
Dip (degrees)

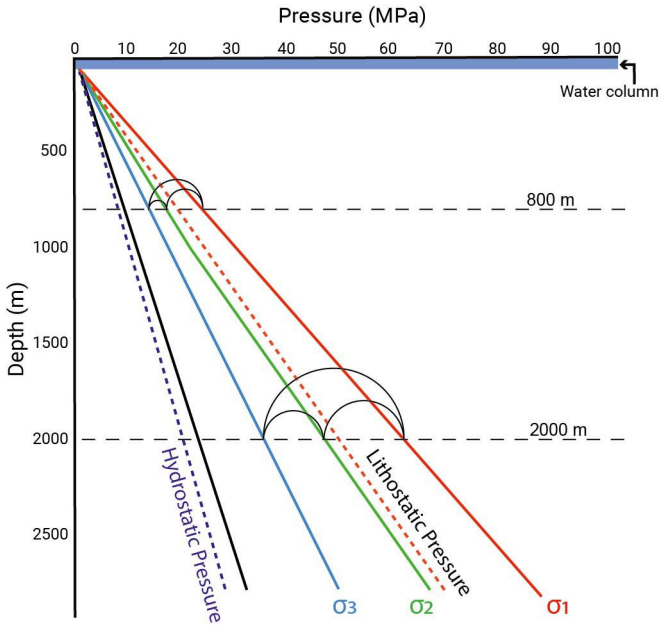
Pressure (MPa)
0
10
20
30
40
50
60
70
80
90
100
Water column
500
800 m
1000
Depth (m)
1500
2000
2000 m
2500
Hydrostatic Pressure
Lithostatic Pressure
σ3
σ2
σ1

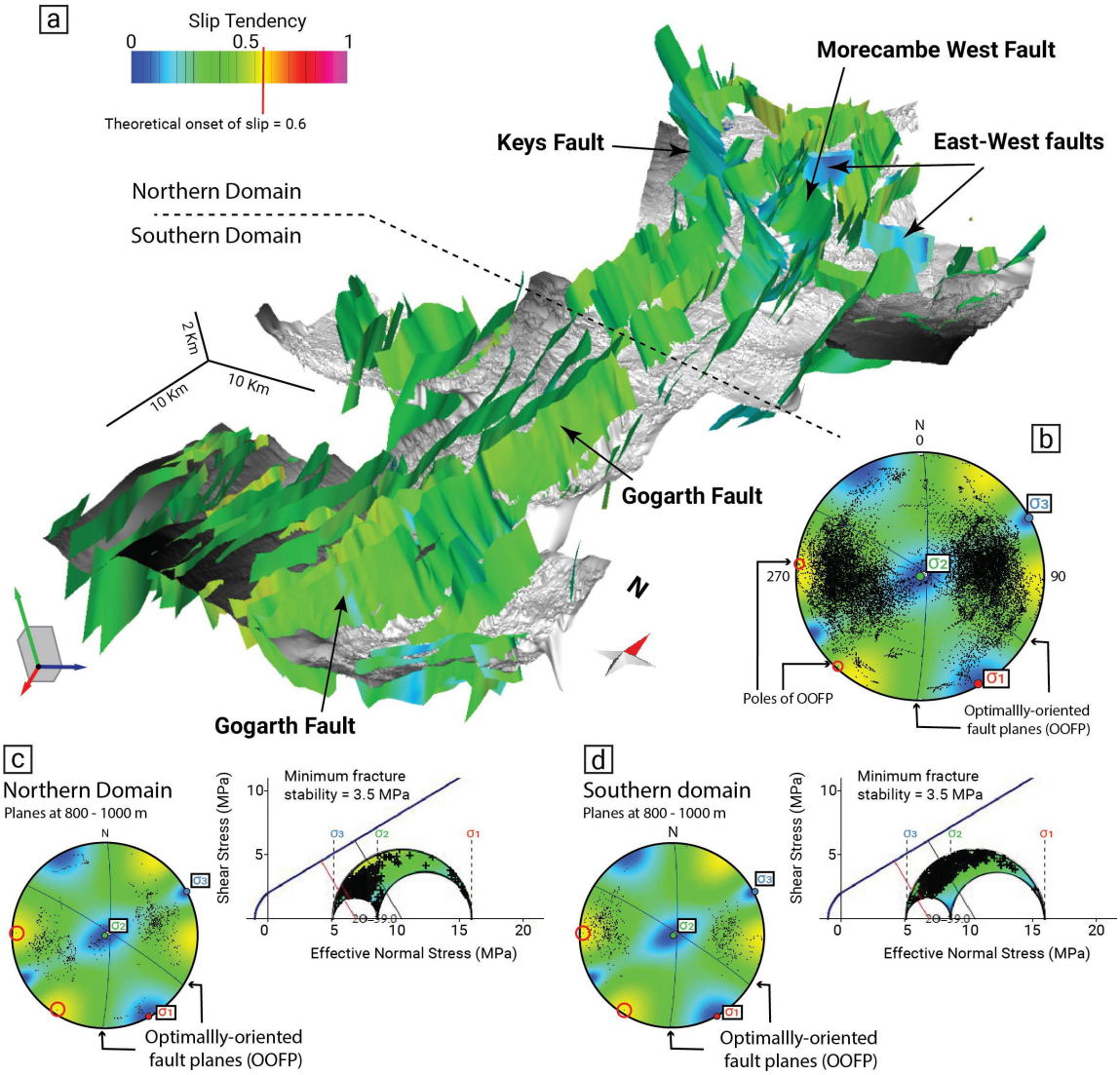
a
Slip Tendency
0
0.5
1
Theoretical onset of slip = 0.6
Morecambe West Fault
Keys Fault
East-West faults
Northern Domain
Southern Domain
2 Km
10 Km
10 Km
Gogarth Fault
Gogarth Fault
N
b
N
0
270
90
Poles of OOFP
Optimallly-oriented
fault planes (OOFP)

c
Northern Domain
Planes at 800 - 1000 m
N
Minimum fracture
stability = 3.5 MPa
Shear Stress (MPa)
Effective Normal Stress (MPa)
Optimallly-oriented
fault planes (OOFP)

d
Southern domain
Planes at 800 - 1000 m
N
Minimum fracture
stability = 3.5 MPa
Shear Stress (MPa)
Effective Normal Stress (MPa)
Optimallly-oriented
fault planes (OOFP)

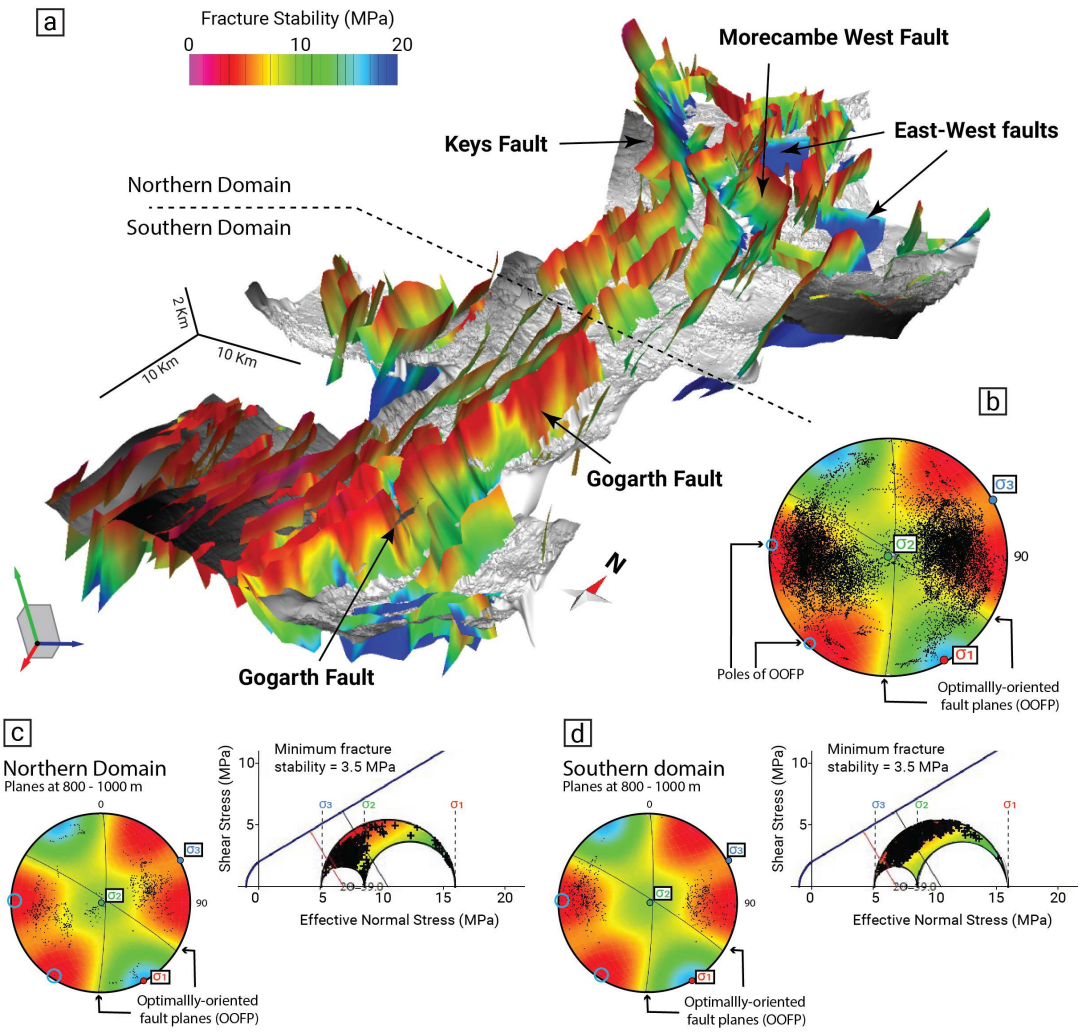
a
Fracture Stability (MPa)
0
10
20
Morecambe West Fault
Keys Fault
East-West faults
Northern Domain
Southern Domain
2 Km
10 Km
10 Km
Gogarth Fault
Gogarth Fault
N
b
σ3
σ2
σ1
90
Poles of OOFP
Optimallly-oriented
fault planes (OOFP)
c
Northern Domain
Planes at 800 - 1000 m
0
90
σ3
σ2
σ1
Optimallly-oriented
fault planes (OOFP)
Minimum fracture
stability = 3.5 MPa
Shear Stress (MPa)
10
5
0
5
10
15
20
Effective Normal Stress (MPa)
d
Southern domain
Planes at 800 - 1000 m
0
90
σ3
σ2
σ1
Optimallly-oriented
fault planes (OOFP)
Minimum fracture
stability = 3.5 MPa
Shear Stress (MPa)
10
5
0
5
10
15
20
Effective Normal Stress (MPa)

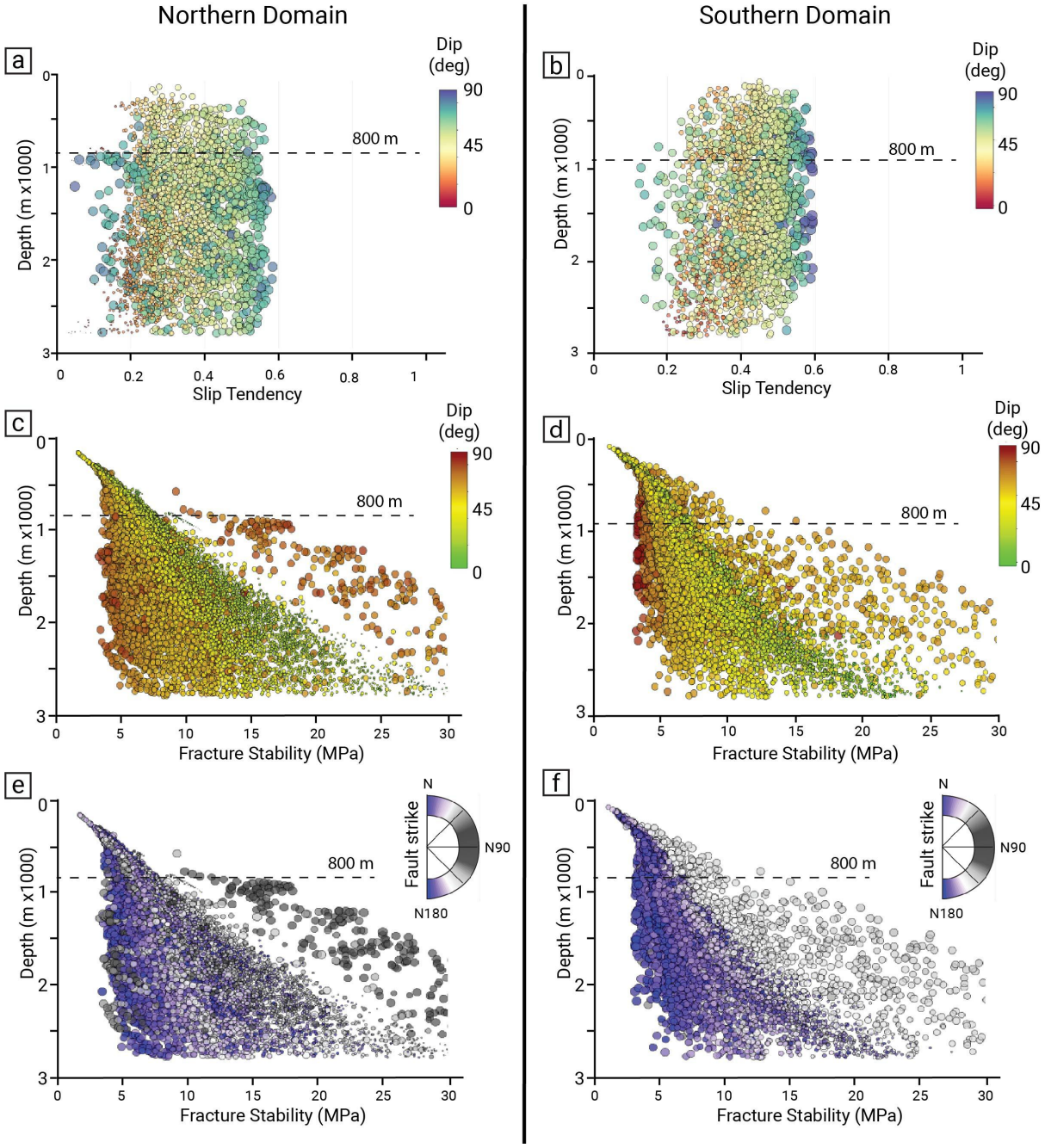
Northern Domain
Southern Domain
a
b
c
d
e
f
Dip (deg)
90
45
0
800 m
Depth (m x1000)
Slip Tendency
Fracture Stability (MPa)
Fault strike
N
N90
N180

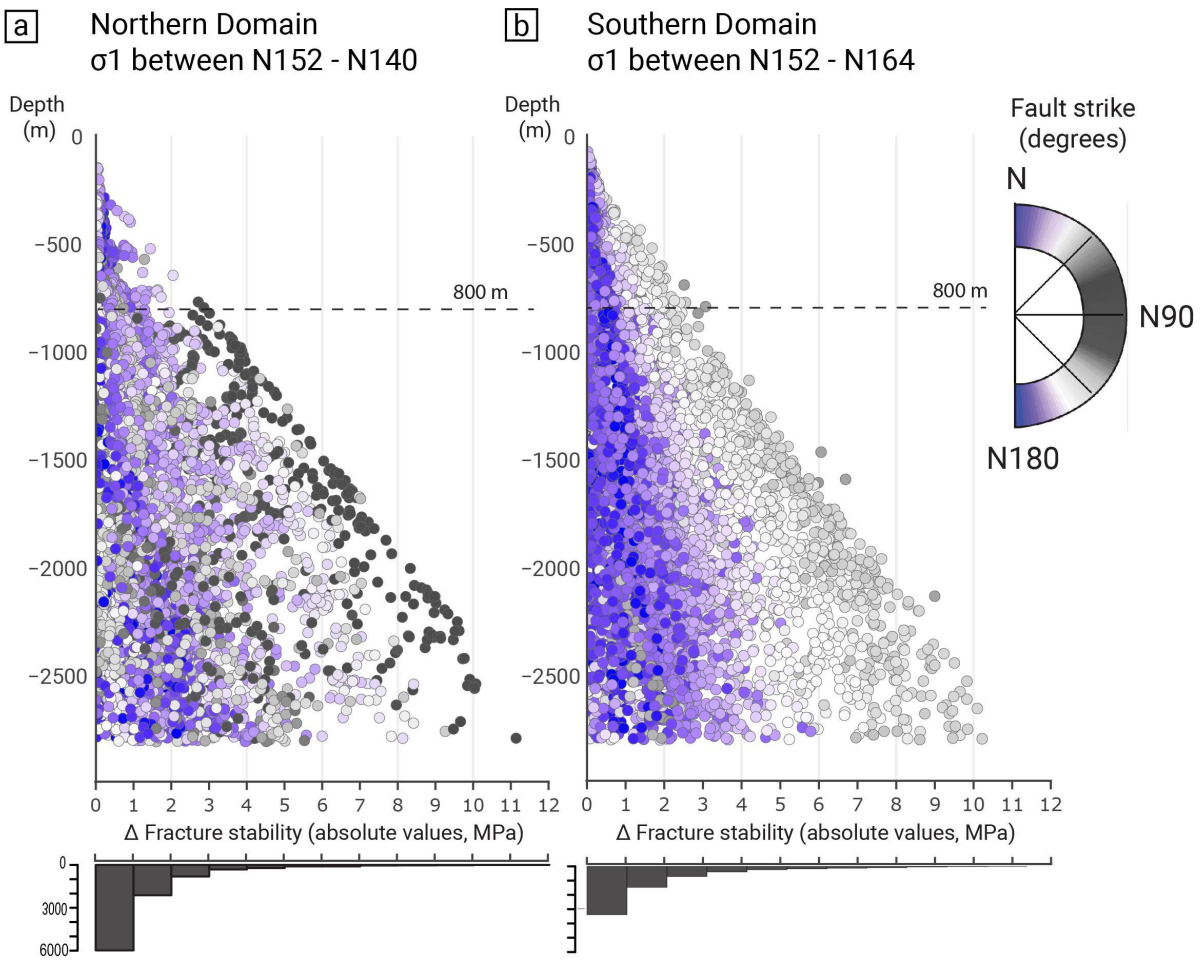
a
Northern Domain
σ1 between N152 - N140
b
Southern Domain
σ1 between N152 - N164
Depth (m)
0
−500
−1000
−1500
−2000
−2500
800 m
0 1 2 3 4 5 6 7 8 9 10 11 12
Δ Fracture stability (absolute values, MPa)
0
3000
6000
Fault strike (degrees)
N
N90
N180

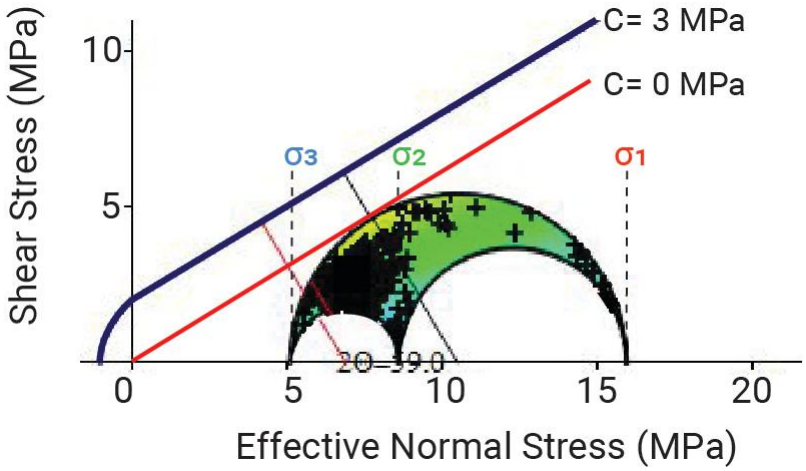
C= 3 MPa
C= 0 MPa
σ3
σ2
σ1
2θ=39.0
Shear Stress (MPa)
Effective Normal Stress (MPa)
0
5
10
15
20
10
5